Computation of Sharp-Fin-Induced Shock Wave/Turbulent Boundary-Layer Interactions

C.C. Horstman*
NASA Ames Research Center, Moffett Field, California

Solution of the Reynolds-averaged Navier-Stokes equations are presented and compared with a family of experimental results for the three-dimensional interaction of a sharp-fin-induced shock wave with a turbulent boundary layer. The solutions predict most of the essential features of the flowfields for various shock wave strengths. However, some features of the measured flowfields, such as secondary separation and the size of the largest separated zones were not accurately computed. The computed flowfields, aided by particle tracing techniques, display a prominent vortical structure that can be correlated with the observed surface phenomena.

Nomenclature

L_s = length along inviscid shock from leading edge of model (see Fig. 9)
L_u = upstream influence length measured in freestream direction (see Fig. 9)
L_{un} = upstream influence length measured normal-to-inviscid shock wave
P_w = wall pressure
P_∞ = freestream static pressure
x,y,z = streamwise, normal, and cross-flow coordinates measured from fin apex (see Fig. 1)
xs = streamwise coordinate measured from inviscid shock wave
$\Delta x, \Delta z$ = distance from fin apex to virtual origin (see Fig. 9)
α = fin angle (see Figs. 1 and 9)
β_0 = inviscid shock angle (see Fig. 9)
β_s = separation angle (see Fig. 9)
β_u = upstream influence angle (see Fig. 9)
δ_0 = boundary-layer thickness at leading edge of fin

Introduction

THREE-DIMENSIONAL, separated flowfields generated by the interaction of a swept shock wave with a turbulent boundary layer at supersonic speeds occur in many types of aircraft and missile configurations. They may be unintentional features of some flowfields or they may be deliberately introduced; but, in all cases, such flows can have a significant effect on the vehicle design or performance. Thus, the prediction of complex, three-dimensional, turbulent, separated flowfields is of primary concern to the designer. One simple geometry that produces a complex three-dimensional shock wave/turbulent boundary-layer interaction consists of a sharp fin mounted on a flat-plate surface (Fig. 1). This type of flowfield occurs in many vehicle configurations of practical importance, such as airbreathing engine inlets, a wing/body juncture, and the intersection of several supersonic control surfaces.

A sharp-fin configuration has been investigated experimentally and computationally over a wide range of conditions. For the most part, the turbulent flow studies have been limited to relatively weak interactions with an unseparated flow or flow near an area of incipient separation. Previous computational results[1-3] solving the Reynolds-averaged Navier-Stokes equations for these weak-interaction flowfields were in good agreement with the experimental results. These computations used algebraic turbulence models and relatively coarse grids. New experimental results[4,5] are now available in which the sharp-fin angle α is systematically varied from the lower values used in previous studies to values high enough to give strong interaction flowfields dominated by separated flow. While these data include only surface measurements, several important observations can be made. As the fin angle (shock wave strength) is increased, the surface flow features remain qualitatively similar to those observed at lower angles, with the size of the interaction increasing with the shock strength. A secondary separation is observed to appear and disappear as α is increased. Finally, the principles of both quasiconical similarity and upstream-influence scaling hold throughout the α range.[5] The question remains as to whether computations using relatively coarse mesh systems and isotropic eddy/viscosity/turbulence models can predict these experimental features as α increases.

This paper presents a parametric computational investigation of the sharp-fin-induced, shock wave/boundary-layer interaction flowfield. Solutions to the Reynolds-averaged Navier-Stokes equations have been obtained for several values of the sharp-fin angle and upstream boundary-layer thickness. These results are compared with the experimental data. Further, these solutions are examined in detail to investigate the physical mechanisms dominating these flowfields. The formation of a vortex-type separation and the relationship between the surface pressure distributions and skin-friction lines as well as the resulting flowfield structure are discussed.

Solutions to the Navier-Stokes Equations

The partial differential equations used to describe the mean flowfield are the time-dependent, Reynolds-averaged, Navier-Stokes equations for a three-dimensional fluid. For turbulence closure, the two-equation, $k-\epsilon$, eddy-viscosity model[6] with wall function boundary conditions[7] is used. The complete equations are described in Refs. 6–8. The numerical procedure chosen here is the MacCormack explicit, second-order predictor-corrector, finite volume method.[9]

The computational domain consisted of uniform mesh spacing in the streamwise direction. In the vertical and cross-flow directions, a geometrically stretched spacing was used near the solid surfaces, followed by a uniform spacing. The total mesh size was 64 points in the streamwise x direction, 32 points in the vertical y direction, and 44 points in the cross-flow z direc-

Received Aug. 1, 1985; revision received Jan. 13, 1986.

*Assistant Branch Chief. Associate Fellow AIAA.

tion. The size of the uniform spacing, which was the same for all three directions, was 0.5 cm for the thick boundary-layer solutions ($\sim 0.39\ \delta_0$) and 0.3 cm for the thin boundary-layer solutions ($\sim 0.83\ \delta_0$). Typically, 16 mesh points were used to resolve the flat-plate boundary layer and 12 points for the boundary layer on the sharp fin.

The upstream boundary conditions were prescribed by a combination of uniform freestream conditions and the results of a boundary-layer computation matching the experimental displacement thickness. At the downstream boundary, the gradients of the flow variables in the streamwise direction were set to zero. In the cross-flow direction, symmetric conditions were applied at $z=0$ ahead of the fin (five streamwise grid points) and zero gradients in the z direction at the other side. At the fin and plate surfaces, no-slip and constant wall temperature conditions were applied. The turbulent kinetic energy and dissipation were set to zero at the surfaces. At the upper boundary, zero gradients in the y direction were applied.

To reduce the CPU time required to achieve a converged solution while using the explicit algorithm, wall function boundary conditions were used at the fin and plate surfaces. The compressible two-dimensional wall functions developed by Viegas et al.[7] were extended to three-dimensional flows for the present solutions. The extension was achieved by replacing the horizontal velocity in the expressions derived in Ref. 7 by the total velocity parallel to the wall. It was also assumed that the flow direction remained constant between the surface and the first grid point away from the surface. Although measurements of yaw angle were not available for $y^+ < 100$ for supersonic high-Reynolds-number flowfields,[8] previous calculations integrating to the wall had shown this to be a reasonable assumption.[10] Near the fin/plate junction, a weighted value ($1/d = 1z + 1/y$) was used to define the distance from the surface. The resulting values of y^+ for the first grid point where 15–100 on the plate and 60–100 for z^+ on the fin. For two-dimensional flows with and without separation, the use of wall functions gave results as good as, and in most cases better than, the results obtained by integrating to the wall.[7]

Results and Discussion

New experimental data for the sharp-fin shock wave/turbulent boundary-layer interaction are now available from two sources.[4,5] Both experimentors varied the fin angle from weak interaction flow regimes near incipient separation to strong interaction regimes with large separated zones. The reported measurements include surface pressure and shear line patterns. In general, the results and conclusions reached in each investigation were the same. Zheltovodov's test matrix included Mach numbers of 2–4 and fin angles of 0–31 deg at a single Reynolds number. Goodwin[5] varied the unit Reynolds numbers, initial boundary-layer thicknesses, and fine angles of 12–22 deg at a constant Mach number (~ 3). Goodwin's data and test conditions were chosen for the present study, since they were the most complete data available in the published literature.

Twelve solutions for the sharp-fin interaction flow were obtained for a single-unit Reynolds number (6.3×10^7/m), a Mach number of 2.94, two boundary-layer thicknesses, and fin angles of 10, 12, 14, 16, 18, and 20 deg, which duplicated the experimental test conditions described in Ref. 5. In general, the computed surface shear line patterns and pressure distributions showed the same qualitative features as the experimental data. Quasiconical flows were observed for the thin boundary-layer cases that were in agreement with the experimental data. The large, primary-separation zones were found via computation and measurement, but no secondary separation was predicted for the thin boundary-layer cases in which incipient secondary separation was experimentally observed. The magnitude of the upstream influence was correctly predicted for the thick boundary-layer cases but not for the thin cases, indicating that the computations did not correctly predict the effect of boundary-layer thickness. Some features of the measured pressure distributions were not accurately computed. In the following paragraphs, typical comparisons between the computed and measured results will be shown to illustrate these areas of agreement and disagreement.

A schematic diagram of the surface features of these interactions as determined from the experimental surface shear lines is shown in Fig. 2. The upstream influence line is defined where the shear lines are first deflected from their original trajectories. Downstream of the upstream influence line, a line of separation (shear line convergence) can be seen clearly. Near the fin, an attachment line can be identified. Between the lines of separation and attachment, a second line of convergence developed as an incipient secondary separation region. This region was observed at fin angles of 12–18 deg for the thin boundary-layer cases only.

Computed surface shear patterns for three thin boundary-layer cases are shown in Figs. 3–5 for fin angles α of 12, 16, and 20 deg, respectively. The computed patterns are similar to

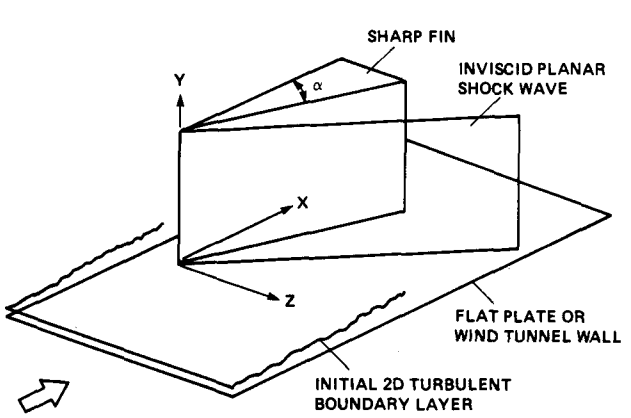

Fig. 1 Flow geometry.

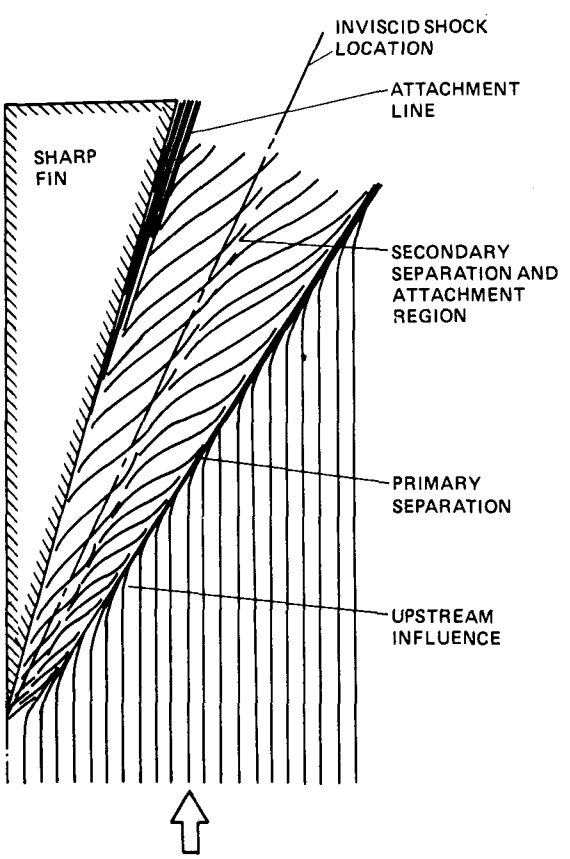

Fig. 2 Experimental surface features.

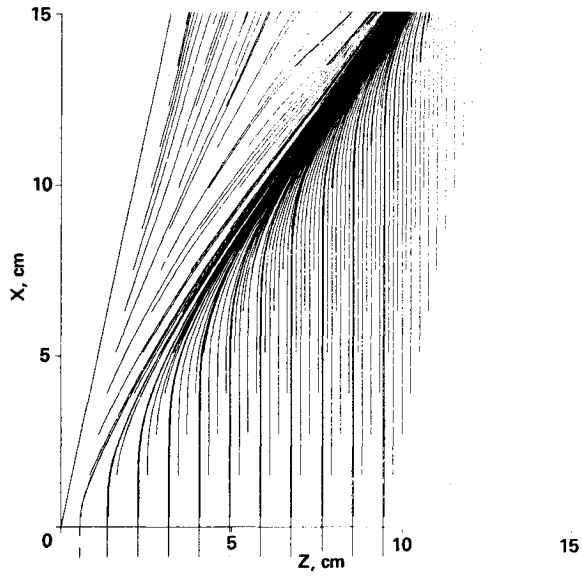

Fig. 3 Computed surface shear lines ($\alpha = 12$ deg, $\delta_0 = 0.36$ cm).

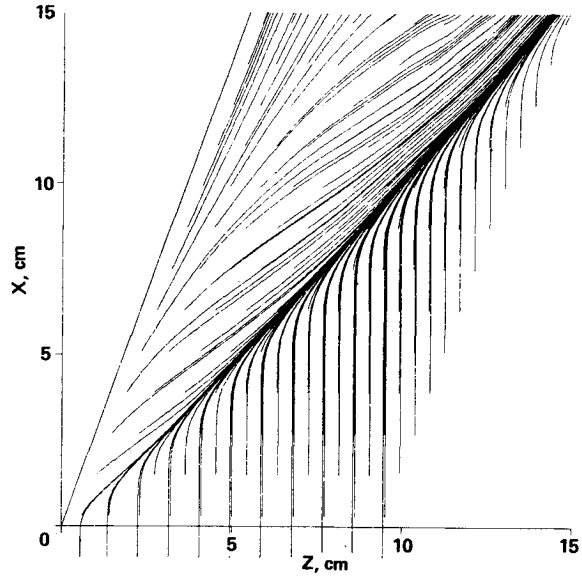

Fig. 5 Computed surface shear lines ($\alpha = 20$ deg, $\delta_0 = 0.36$ cm).

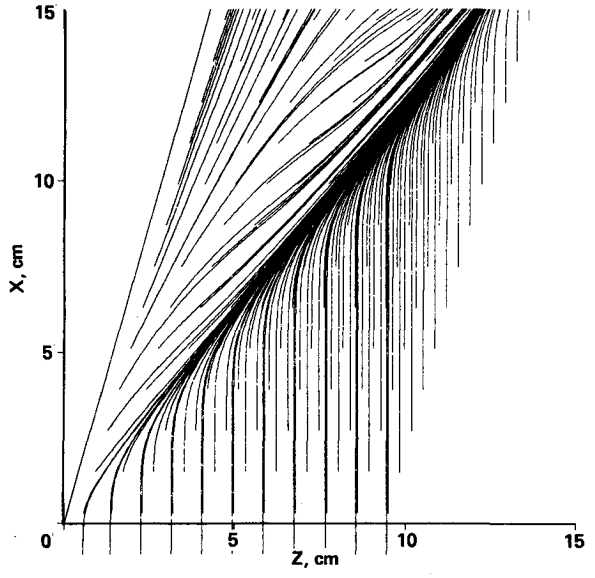

Fig. 4 Computed surface shear lines ($\alpha = 16$ deg, $\delta_0 = 0.36$ cm).

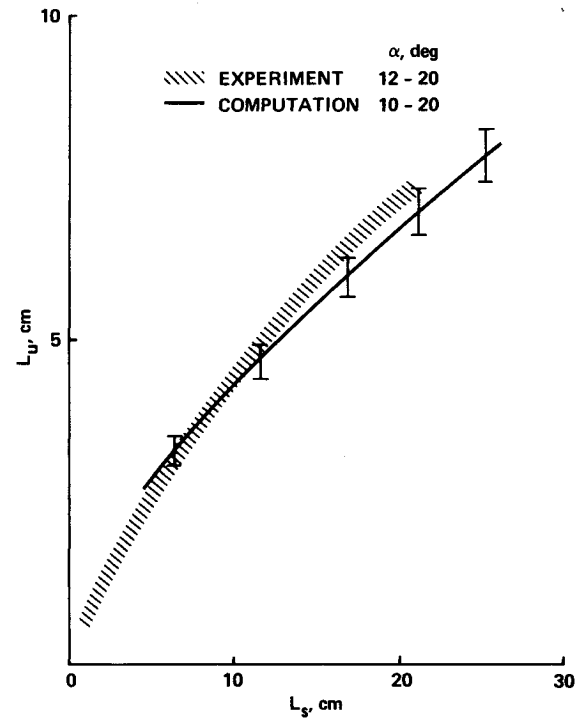

Fig. 6 Effect of shock strength on upstream influence ($\delta_0 = 1.3$ cm).

the measured patterns except for the absence of secondary separation. Possible reasons for this deficiency will be discussed later. As the fin angle increases, the size of the primary separation region increases dramatically. The computed patterns for the thick boundary-layer cases (not shown), which are similar, are in good agreement with experiment results (neither showed a secondary separation region).

The computed and experimental upstream influence distances are compared in Figs. 6-8 for both the thin and thick boundary-layer cases. The distances L_u and L_s are defined in Fig. 9. For the thick boundary-layer cases, the measured and computed upstream-influence distances are in good agreement (Fig. 6). At large distances from the fin apex (large L_s), the computed results slightly underpredict the measured values. When plotted in this manner (L_u vs L_s), the results for all values of α (both computed and measured) collapse into a single curve. However, if L_{un} (the upstream-influence distance normal to the inviscid shock wave) were plotted, L_{un} would increase with increasing α since $L_{un} = L_u \sin\beta_0$ and β_0 (the inviscid shock angle) increases with α.

The upstream-influence lengths for the thin boundary-layer cases are compared in Fig. 7. Although the computed values of L_u collapse independently of α, similar to the measured values, the magnitudes of the calculated values are up to 20% less than the measured values.

The thin and thick boundary-layer cases are compared for $\alpha = 18$ deg on Fig. 8. This clearly shows that the predicted sensitivity of the upstream influence as a function of δ_0 is incorrect. It is not known why the computed results fail to predict these trends with δ_0. Two differences are noted between the computed results for the thin and thick boundary-layer cases: 1) the mesh resolution in the x and z directions is twice as fine for the thick boundary-layer case when compared to the local boundary-layer thicknesses for each case; and 2) most of the flowfield for the thick boundary-layer cases was in the inception zone (Fig. 9), where the extent of the separation zone is only a few δ_0 and, for the thin cases (mostly in the conical flow zone), the separation zone is much larger in terms of δ_0.

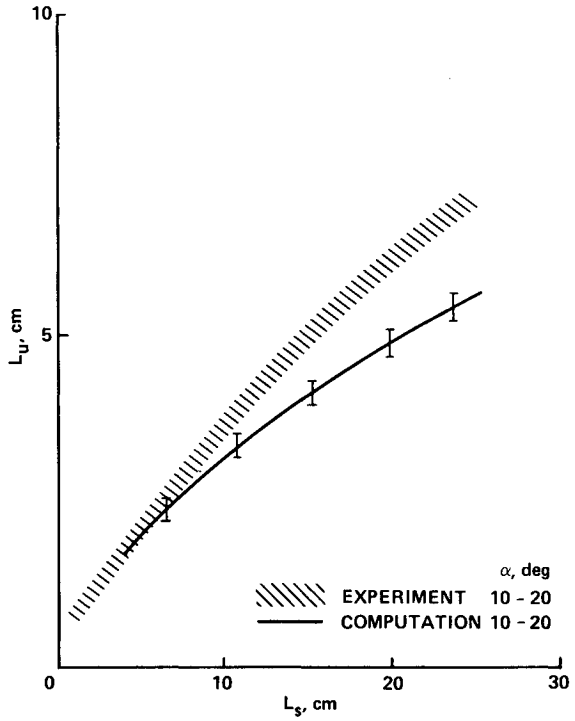

Fig. 7 Effect of shock strength on upstream influence ($\delta_0 = 0.36$ cm).

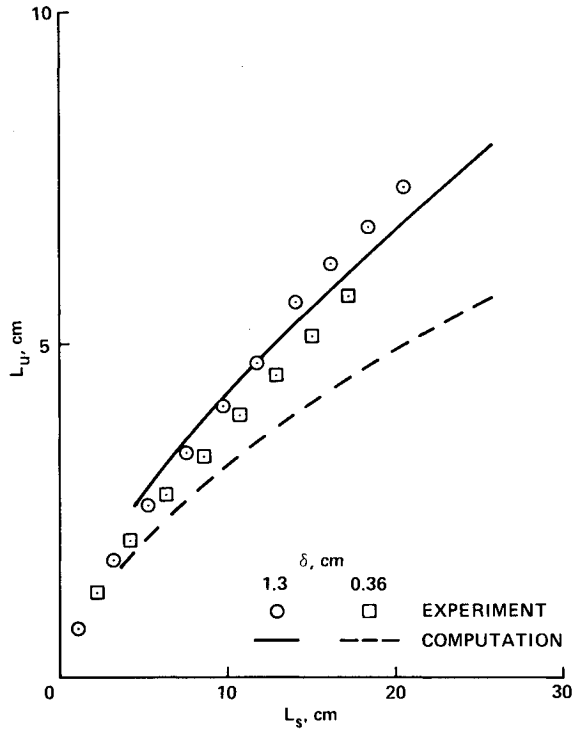

Fig. 8 Effect of boundary-layer thickness on upstream influence ($\alpha = 18$ deg).

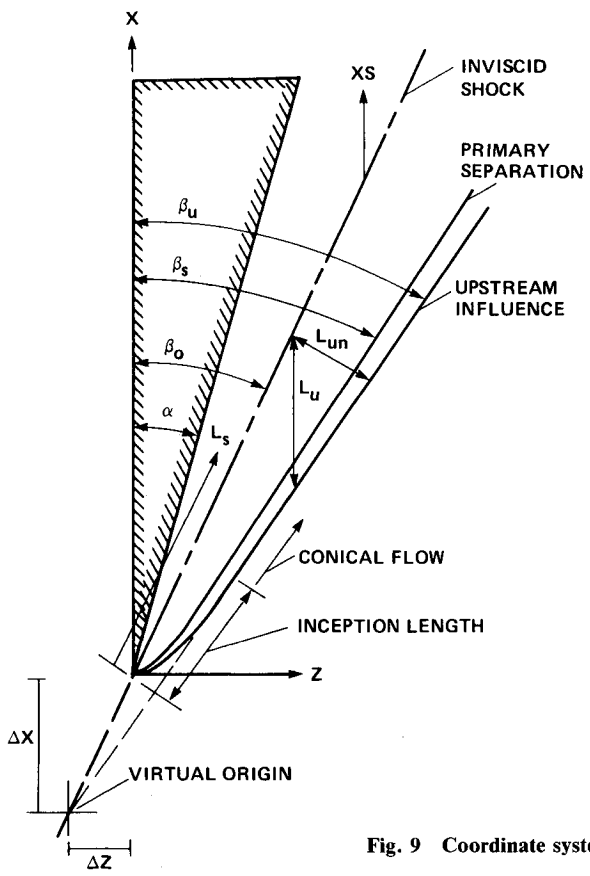

Fig. 9 Coordinate systems.

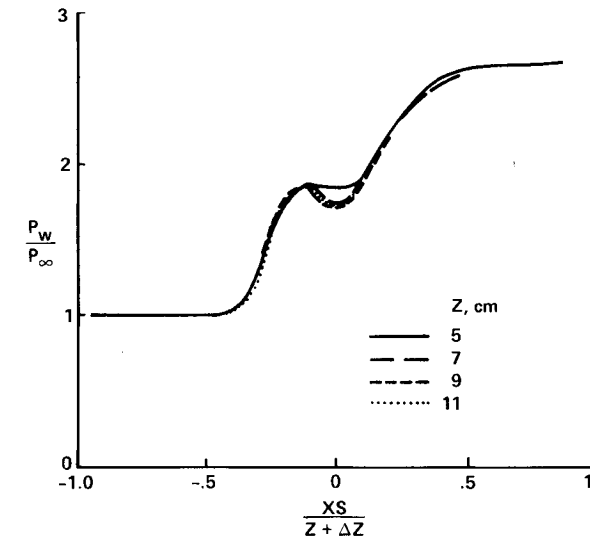

Fig. 10 Computed quasiconical similarity ($\alpha = 14$ deg, $\delta_0 = 0.36$ cm).

Previous investigations have shown that the agreement between computed and experimental results tends to deteriorate as the extent of the separation zone normalized by δ_0 increases.[8,10]

Quasiconical flow was observed experimentally for all values of α for the thin boundary-layer cases. Therefore, all measured flow properties indicate conical flow similarity from a virtual origin after an initial inception length (Fig. 9). The measurements also showed that the inception length extended over most of the flowfield for the thick boundary-layer cases. The computed results were in agreement with these findings. One criterion used to show conical flow[5] was to plot several streamwise pressure distributions in conical coordinates and see if they collapsed to a single curve. Two examples ($\alpha = 14$ and 20 deg) of the computed thin boundary-layer pressure distributions are shown in Figs. 10 and 11. Conical flow is evident for values of z greater than 6 cm (similar to the experimental results).

When quasiconical flow is present for these flowfields, the size of the interaction can be described by angular measurements alone. β_u and β_s are the angles describing the upstream influence and primary separation lines (Fig. 9),

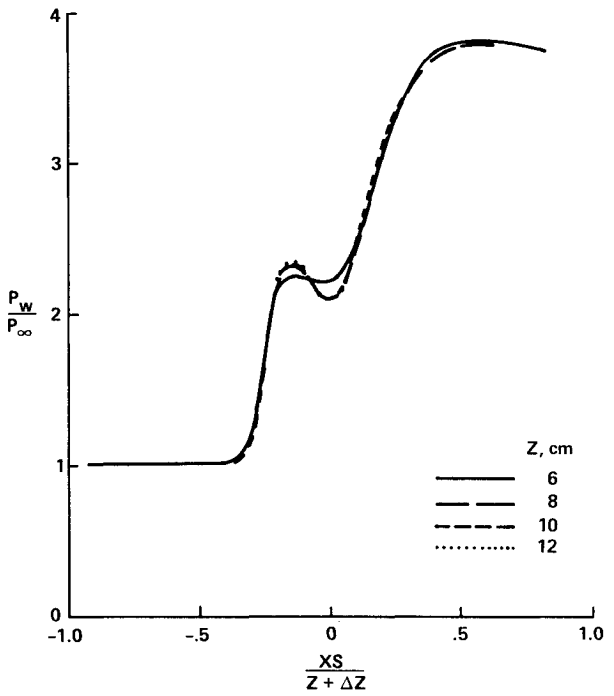

Fig. 11 Computed quasiconical similarity ($\alpha = 20$ deg, $\delta_0 = 0.36$ cm).

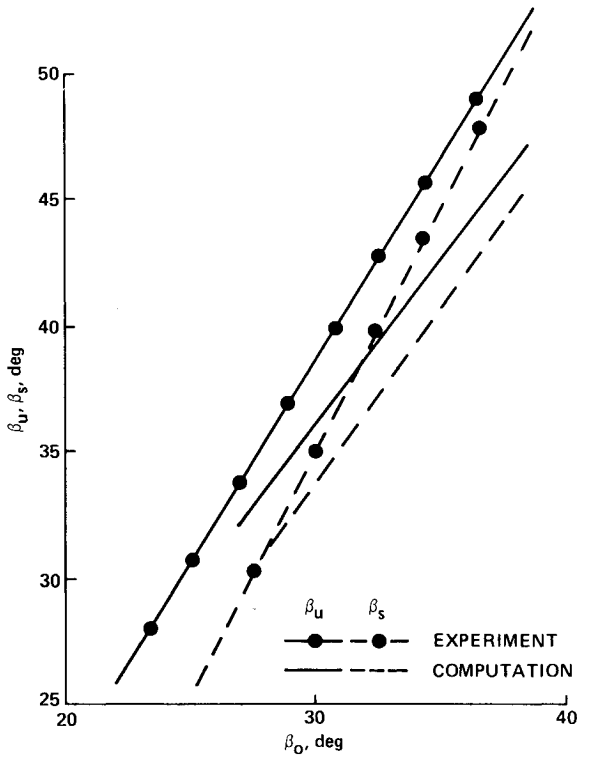

Fig. 12 Comparison of surface feature angles ($\delta_0 = 0.36$ cm).

respectively. The computed angles are compared with the experimental values in Fig. 12 for the thin boundary-layer cases. β_u is determined from both the computed pressure distributions and surface shear line angles. The upstream-influence location is defined where the turning angle of the surface shear lines is 2.5 deg or the pressure rise is 10%. Both methods give the same value of β_u. β_s is measured from the surface shear line patterns (Figs. 3–5). Comparison of the results shows that the computed values of β_u and β_s are less than the measured values, especially at the higher values of β_0 (large fin angles).

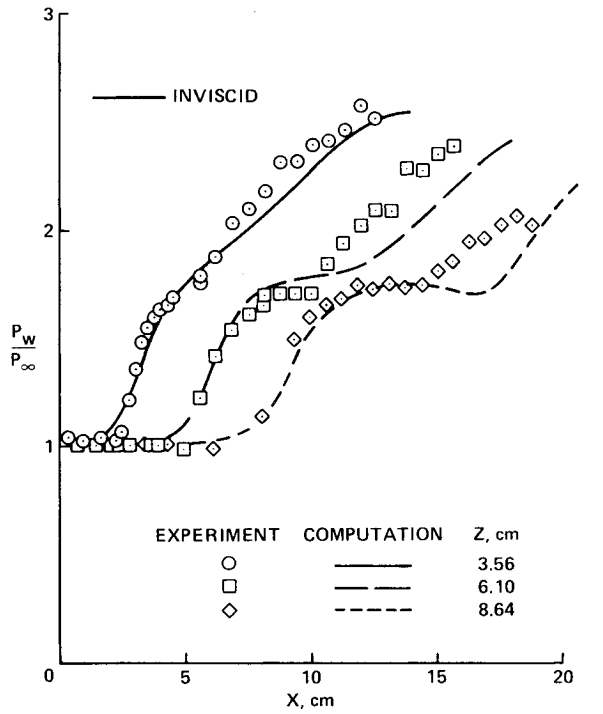

Fig. 13 Comparison of surface pressure distributions ($\alpha = 14$ deg, $\delta_0 = 1.3$ cm).

Therefore, the stronger the interaction and the extent of separation are, the larger the disagreement between the computations and experiment. Thus, the slopes of β_u and β_s vs β_0 are underpredicted. These comparisons are another way of showing the differences seen in Fig. 7. Also note that, as β_0 increases, both the computed and measured values of β_u approach their respective values of β_s (although not at the same rate).

A few typical comparisons between the computed and measured surface pressure distributions are shown in Figs. 13 and 14 for thick boundary-layer cases and in Figs. 15 and 16 for thin boundary-layer cases. Figure 13 compares the results for $\alpha = 14$ deg and Fig. 14 for $\alpha = 20$ deg. In general, the overall features of the measured distributions are as predicted, in particular, regarding the location of the initial pressure rise. This is consistent with the upstream-influence results (Fig. 6). For the thin boundary-layer cases (Figs. 15 and 16), comparisons are made for $\alpha = 14$ and 18 deg, respectively. (Complete pressure data are not available for $\alpha = 20$ deg.) The computations again predict the overall features of the measured distributions, but not the streamwise extent of the pressure plateaus. The computed initial pressure rise is downstream of the measured locations. The experimental data show a pressure overshoot over the final inviscid pressure level, whereas the computations do not. For both the thin and thick boundary-layer cases, the predicted pressure plateau levels are greater than the measured ones for the larger fin angles (Figs. 14 and 16). It will be shown in the next section that these sharp-fin interaction flows are dominated by a vortex-type separation. The predicted size and strength of the vortex structures may be smaller that the ones present in the thin boundary-layer experimental (test) flows. If a larger vortex structure were computed, the streamwise extent of the pressure plateau would increase as well as the upstream influence.

Computational Flowfield

The flow structure in the computational flowfield can be examined and connected with the surface features such as the shear line patterns and pressure distributions by using particle path tracing techniques.

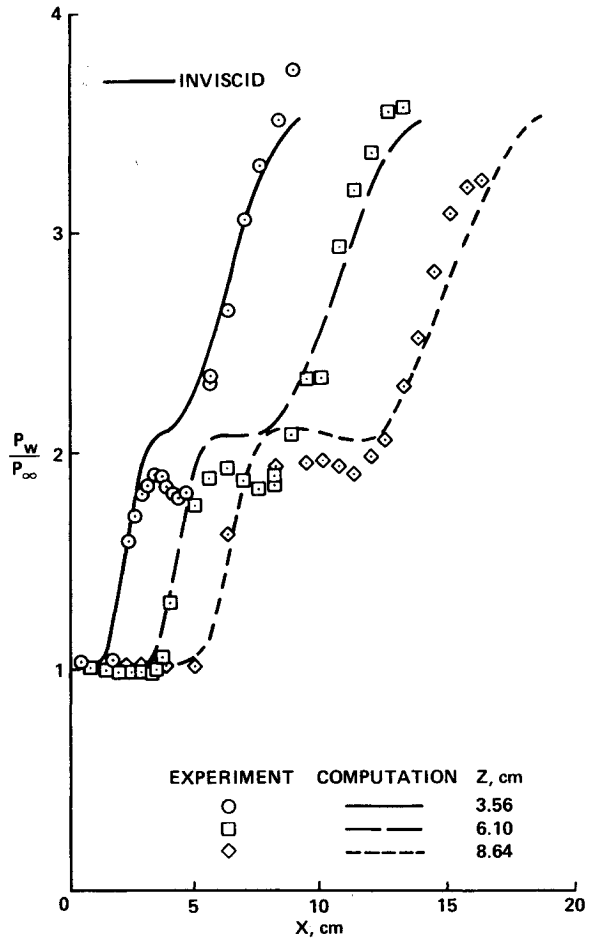

Fig. 14 Comparison of surface pressure distributions ($\alpha = 20$ deg, $\delta_0 = 1.3$ cm).

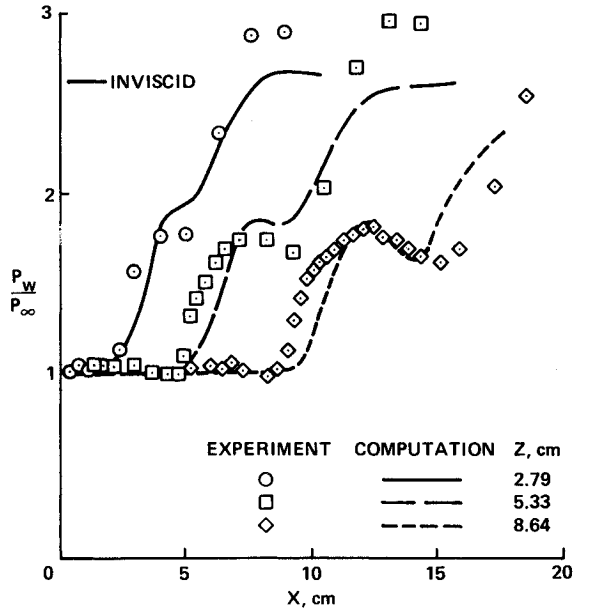

Fig. 15 Comparison of surface pressure distributions ($\alpha = 14$ deg, $\delta_0 = 0.36$ cm).

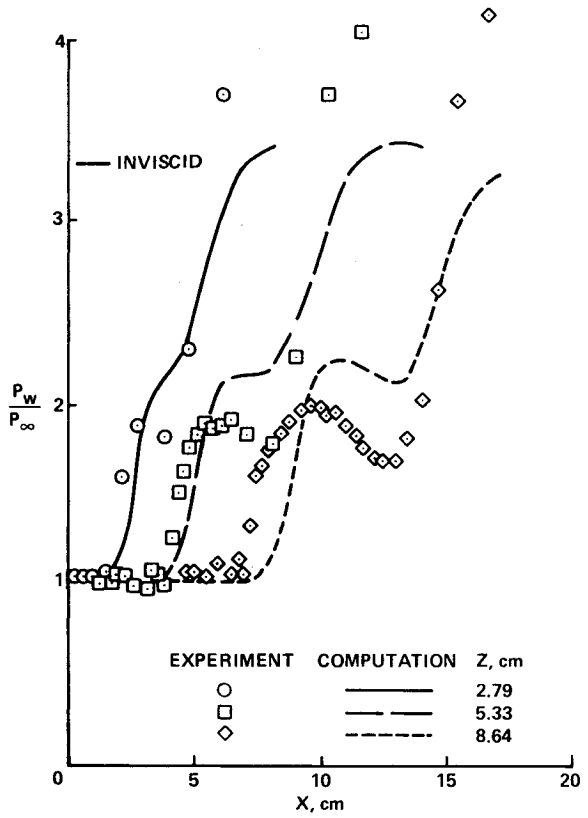

Fig. 16 Comparison of surface pressure distributions ($\alpha = 18$ deg, $\delta_0 = 0.36$ cm).

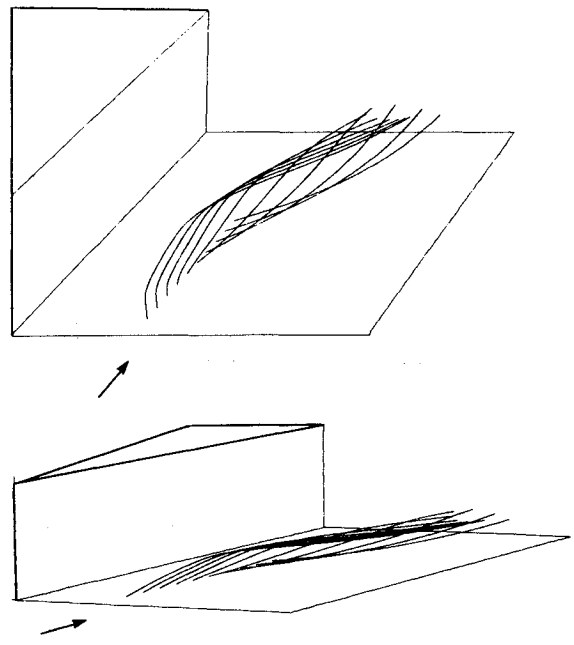

Fig. 17 Computed particle path trajectories, three-dimensional views ($\alpha = 20$ deg, $\delta_0 = 0.36$ cm).

Typical three-dimensional particle paths are shown in Figs. 17 and 18 for the $\alpha = 20$ deg, thin boundary-layer case. Two three-dimensional views are shown in Fig. 17 and a plan and side view in Fig. 18. The particles are started along a line parallel to the fin surface spanning the separation line at $y/\delta_0 = 0.25$. A roll-up into a vortex is seen, which is the principal mechanism for these three-dimensional separations. The particles starting upstream of the separation line first rise and then, as they are swept into the vortex, pitch down and rotate. The particles starting downstream of the separation line continually rise and rotate. Similar vortex structures are also observed for the other fin angles ($\alpha = 10$-18 deg) and for the thick boundary-layer cases.

As noted previously, the flowfields are quasiconical for the thin boundary-layer cases. Also, it has been shown experimentally that the thick boundary-layer case also becomes quasiconical if the measurements extend sufficiently far

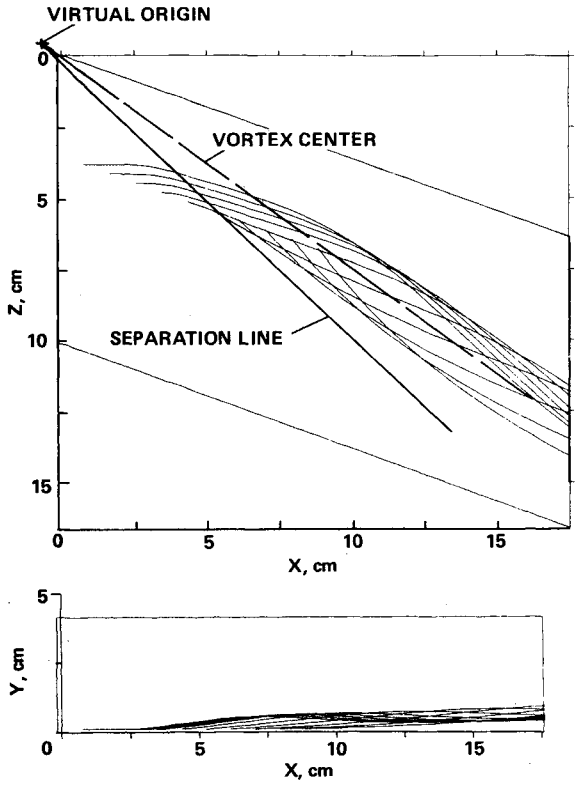

Fig. 18 Computed particle path trajectories, plan and side views ($\alpha = 20$ deg, $\delta_0 = 0.36$ cm).

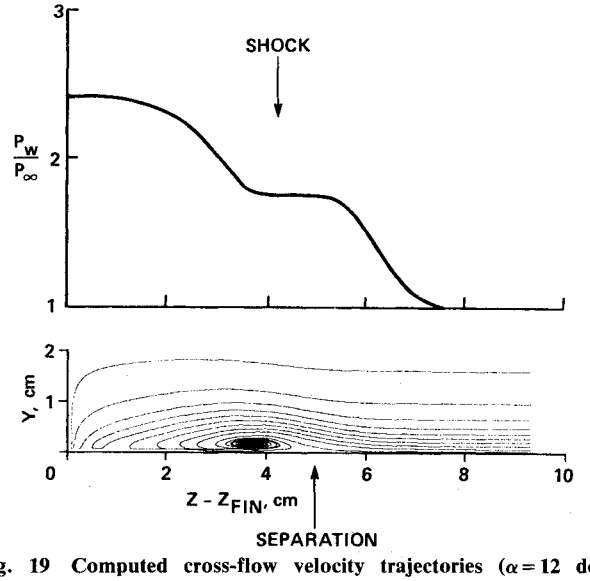

Fig. 19 Computed cross-flow velocity trajectories ($\alpha = 12$ deg, $\delta_0 = 0.36$ cm).

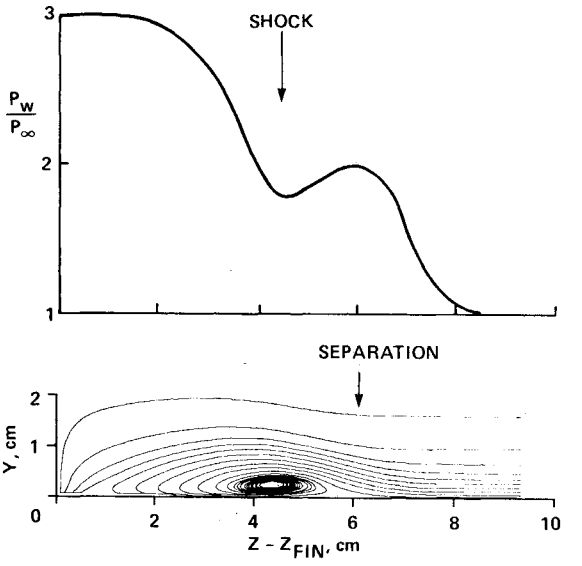

Fig. 20 Computed cross-flow velocity trajectories ($\alpha = 16$ deg, $\delta_0 = 0.36$ cm).

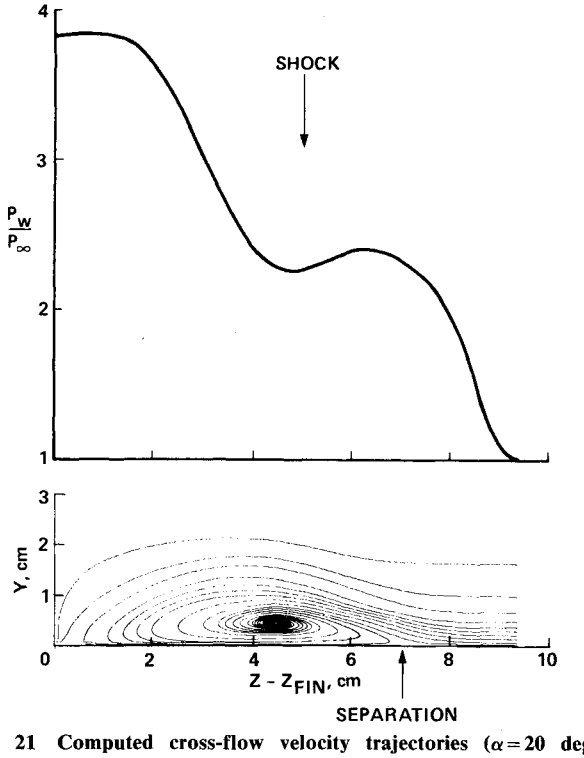

Fig. 21 Computed cross-flow velocity trajectories ($\alpha = 20$ deg, $\delta_0 = 0.36$ cm).

downstream.[11] However, the computational domain was not extended this far. Also note that a line through the vortex center will pass through the virtual origin near the fin apex (Fig. 18, plan view). To further examine the vortical structures, let us look at the particle paths confined to a two-dimensional plane with the cross-flow velocities calculated in approximate conical coordinates, i.e., $w\cos\theta - u\sin\theta$ vs v, where θ is the angle of the line in the x-z plane passing through the point of interest and the virtual origin. Examples of these special trajectories for the thin boundary-layer cases are shown in Figs. 19-21 for $\alpha = 12$, 16, and 20 deg, calculated in the $x = 11.85$ cm plane. The corresponding pressure distributions are also shown for each case. The locations of the inviscid shock and separation (from Figs. 3-5) are indicated.

We can now identify many features of the flowfield. The separation line is closely related to the vortex roll-up. An attachment region near the fin is observed. The decrease in the surface pressure occurring after the first pressure rise near separation is evidently caused by the vortex. Low pressure under the core of a vortex has also been observed in other flowfields by Hung and Buning[12] and Degani and Schiff.[13] Hung and Buning conclude that the low pressure occurs because of the high reversed velocity resulting from an image effect, or so-called ground effect, of the vortex. The present results show that the size of the vortex increases with increasing shock strength. For $\alpha = 16$ deg, a secondary separation (possibly a second vortex) has been experimentally observed. Its location would place it under the primary vortex shown in Fig. 20. The cross-flow grid spacing for this calculation is 0.3 cm ($\sim 0.83\ \delta_0$). Therefore, it is doubtful that the present

calculations can predict a second small, counterrotating vortex under the primary vortex.

Conclusions

Solutions were obtained for a series of complex, three-dimensional, shock wave/turbulent boundary-layer interaction flowfields using wall function boundary-layer conditions with a two-equation, $k-\epsilon$ turbulence model. The essential features of the interactions were predicted, such as quasiconical flow, but many details were not. With increasing shock strength (larger separation), the predictions progressively became less accurate. In particular, secondary separation for the thin boundary-layer cases was not computed, although it was experimentally observed. Also, the predicted upstream-influence angles were too small. Both the grid resolution and the use of an isotropic eddy/viscosity/turbulence model were possible sources of these disagreements.

Further grid refinement studies are planned, depending on the availability of larger computers. Improvements in the turbulence model are planned with more detailed experimental data, including three-dimensional, shear stress measurements, are available. Further research at NASA Ames Research Center is planned in both areas.

In spite of the computational deficiencies, the computed flowfields were sufficiently accurate to be used to obtain a clear visualization and better understanding of the three-dimensional separation process. This is not possible experimentally, since the high turbulence level in these flowfields masks the mean fluid motion.[8] Using particle tracing techniques, the principal separation mechanism has been found to be a large vortex. As the flowfield structure becomes better known, surface features such as the shear line patterns as pressure distributions will be more easily explained.

References

[1]Horstman, C. C. and Hung, C.-M., "Computation of Three-Dimensional Turbulent Separated Flows at Supersonic Speeds," *AIAA Journal*, Vol. 17, Nov. 1979, pp. 1155-1156.

[2]Knight, D. D., "Modelling of Three-Dimensional Shock Wave Turbulent Boundary Layer Interactions," Paper presented at Conference on Macroscopic Modelling of Turbulent Flows and Fluid Mixtures, INRIA, France, Dec. 1984.

[3]Knight, D. D., "A Hybrid Explicit-Implicit Numerical Algorithm for the Three-Dimensional Navier-Stokes Equations," *AIAA Journal*, Vol. 22, Aug. 1984, pp. 1056-1063.

[4]Zheltovodov, A. A., "Regimes and Properties of Three-Dimensional Separation Flows Initiated by Skewed Compression Shocks," *Zhurnal Prikladnoi Mekhaniki i Tekhnicheskoi Fiziki*, No. 3, May-June 1982, pp. 116-123.

[5]Goodwin, S. P., "An Exploratory Investigation of Sharp Fin-Induced Shock Wave/Turbulent Boundary Layer Interactions at High Shock Strengths," M.Se. Thesis, Princeton University, Princeton, NJ, Nov. 1984.

[6]Jones, W. P. and Launder, B. E., "The Prediction of Laminarization with Two-Equation Model of Turbulence," *International Journal of Heat and Mass Transfer,* Vol. 15, Feb. 1972, pp. 301-314.

[7]Viegas, J. R., Rubesin, M. W., and Horstman, C. C., "On the Use of Wall Functions as Boundary Conditions for Two-Dimensional Separated Compressible Flows," AIAA Paper 85-0180, Jan. 1985.

[8]Settles, G. S., Horstman, C. C., and McKenzie, T. M., "Flowfield Scaling of a Swept Compression Corner Interaction—A Comparison of Experiment and Computation," AIAA Paper 84-0096, Jan. 1984.

[9]MacCormack, R. W., "Numerical Solution of the Interaction of a Shock Wave with a Laminar Boundary Layer," *Lecture Notes in Physics*, Vol. 8, 1972, Springer-Verlag, Berlin, pp. 151-163.

[10]Horstman, C. C., "A Computational Study of Complex Three-Dimensional Compressible Turbulent Flow Fields," AIAA Paper 84-1556, June 1984.

[11]Settles, G. S. and Lu, F. K., "Conical Similarity of Shock/Boundary Layer Interactions Generated by Swept and Unswept Fins," *AIAA Journal*, Vol. 23, July 1985, pp. 1021-1027.

[12]Hung, C-M. and Buning, P. G., "Simulation of Blunt-Fin Induced Shock Wave and Turbulent Boundary Layer Interaction," AIAA Paper 84-0457, Jan. 1984.

[13]Degani, D. and Schiff, L. B., "Computation of Supersonic Viscous Flows Around Pointed Bodies at Large Incidence," AIAA Paper 83-0034, Jan. 1983.